

Magnetar field dynamics shaped by chiral anomalies and helicity

Clara Dehman^{1*} and José A. Pons¹

¹ *Departament de Física Aplicada, Universitat d'Alacant, 03690 Alicante, Spain*

The chiral magnetic effect (CME)—a macroscopic manifestation of the quantum chiral anomaly—induces currents along magnetic field lines, facilitating mutual conversion between chiral asymmetry and magnetic helicity. Although the finite electron mass suppresses chiral asymmetry through spin-flip processes, we demonstrate that the CME remains effective and plays a significant role in the magnetic field evolution of magnetars. The magnetic helicity acts as a persistent internal source of chiral asymmetry, which mediates the redistribution of magnetic energy across spatial scales, without requiring an external energy source. Focusing on the neutron star crust, we show that this mechanism reshapes the magnetic field configuration inherited at birth and, within a hundred years, amplifies both toroidal and poloidal large-scale dipolar components (relevant for spin-down) up to 10^{14} G at the expense of small-scale structures. Our results offer a microphysical mechanism—alternative to traditional hydrodynamic dynamo models—establishing a new framework for understanding magnetar field dynamics.

The origin and evolution of magnetic fields in neutron stars (NSs) – especially magnetars, the class with the strongest known magnetic fields – remain subjects of active debate [1, 2]. It is generally agreed that the large-scale dipolar fields observed in these objects, as inferred from spin periods and period derivatives, cannot be solely attributed to fossil fields inherited from their progenitor stars. Consequently, turbulent dynamo amplification is often invoked to explain their extreme strengths [3–7]. Yet despite extensive study, critical questions persist, particularly regarding how magnetic energy transfers to larger scales, leaving the origin of magnetar fields unresolved.

Beyond macroscopic hydrodynamic processes such as dynamos and turbulence, quantum field theory establishes a fundamental microscopic connection between chirality and helicity through the chiral anomaly. This phenomenon facilitates a two-way transfer between fermionic chiral asymmetry and magnetic helicity. Recent research has increasingly focused on linking the generation of large-scale magnetic fields to chiral asymmetries produced during core-collapse supernovae and the proto-NS phase [8, 9]. However, significant challenges persist, most notably the efficiency of spin-flip scattering processes induced by the finite electron mass, raising doubts about the CME's relevance in these environments. The rapid, temperature-dependent spin-flip reactions reduce the chiral imbalance, constraining the effectiveness of the chiral instability mechanism [10, 11].

The concept that a pre-existing helical magnetic field at short wavelengths could experience an inverse-like cascade driven by chiral asymmetry, ultimately generating large-scale magnetic fields, has been proposed in the context of the early Universe [12–14], but has been considered far less often in stellar environments [9, 15]. In this work, unlike previous studies, we incorporate chiral effects into the study of NSs, explicitly accounting

for spin-flip scattering processes in our numerical simulations. We explore the long-term interaction between magnetic helicity and chiral asymmetry during the early stages of NS evolution. The simulations reveal that, while spin-flip processes significantly suppress chiral effects, residual asymmetries can persist for hundreds of years, enabling sustained energy transfer from small to large scales. In this context, the chiral anomaly acts as a catalyst, potentially reorganizing turbulent magnetic fields—originally generated by dynamo processes—to form a coherent, large-scale dipolar field.

The mechanism operates as follows: a small but sustained imbalance between left- and right-handed electrons generates an electric current parallel to the magnetic field—an effect known as the Adler-Bell-Jackiw anomaly [16, 17]. This imbalance is quantified by the chiral chemical potential $\mu_5 \equiv \mu_R - \mu_L$ ¹, where μ_R and μ_L are the chemical potentials of right- and left-handed electrons, respectively. A non-vanishing μ_5 implies that magnetic field evolution in NS interiors must include an effective chiral degree of freedom, despite being within the Standard Model. When $\mu_5 \neq 0$, Maxwell's equations acquire an additional current term [18]:

$$\mathbf{J}_5 = \frac{\alpha\mu_5}{\pi\hbar}\mathbf{B}, \quad (1)$$

where $\alpha = e^2/\hbar c$ is the fine structure constant, e is the fundamental charge, \hbar is the reduced Planck constant, and c is the speed of light. We use Gaussian units throughout the paper.

In an MHD context, the chiral current (\mathbf{J}_5) acts analogously to a dynamo, amplifying magnetic fields by drawing on the energy stored in the chiral chemical potential. Notably, it can have either sign and reverse the process – tapping magnetic energy to generate chirality. In this letter, we examine this microphysical mechanism as an

* clara.dehman@ua.es

¹ Note that definitions of μ_5 vary in the literature, sometimes differing by a sign [11] or a factor of 2 [15], depending on the source.

alternative – or more precisely, a complement – to classical hydrodynamical dynamos in explaining magnetar fields.

NSs exhibit a complex internal structure with multiple fluid components, each possessing distinct hydrodynamical velocities. In the outer crust, a rigid ionic lattice severely limits ion mobility, allowing only electrons to flow freely and sustain the currents essential for magnetic field evolution. The inner crust introduces added complexity with superfluid neutrons, which partially decouple from the nuclear lattice and act as a neutral fluid component. Complexity peaks in the NS core, where coexisting superfluid neutrons and superconducting protons necessitate a sophisticated multi-fluid framework. Given this complexity, magnetic field evolution is typically studied using region-specific approximations. Here, we focus on the crust, where higher electrical resistivity compared to the core leads to shorter magnetic field evolution timescales—making crustal physics a key region for understanding magnetar activity (ages $\lesssim 10$ kyr). In this regime, where only (slowly drifting) electrons are mobile due to the solid ionic lattice, the Hall-MHD (or e-MHD) approximation applies [19]. Magnetic field evolution is then governed by the induction equation derived from Faraday’s law:

$$\frac{\partial \mathbf{B}}{\partial t} = -c \nabla \times \mathbf{E}, \quad (2)$$

where the electric field accounts for Ohmic dissipation, Hall drift, and the new chiral magnetic contribution:

$$c\mathbf{E} = \eta(\nabla \times \mathbf{B} - k_5 \mathbf{B}) + f_h(\nabla \times \mathbf{B}) \times \mathbf{B}. \quad (3)$$

Here, $\eta = c^2/4\pi\sigma_e$ is the magnetic diffusivity, where σ_e is the electrical conductivity; $k_5 = 4\alpha\mu_5/\hbar c$ is the chiral wavenumber; and $f_h = c/4\pi en_e$ is the Hall prefactor, with n_e the electron number density.

Magnetic field evolution must be coupled to the evolution equation for the chiral number density $n_5 \equiv n_R - n_L$ [10, 20], which includes both source and sink terms:

$$\frac{\partial n_5}{\partial t} = \frac{2\alpha}{\pi\hbar} \mathbf{E} \cdot \mathbf{B} + n_e \Gamma_w^{\text{eff}} - n_5 \Gamma_f. \quad (4)$$

Here, the reaction rate Γ_f accounts for spin-flip interactions and acts as a sink term, while Γ_w^{eff} represents the effective weak reaction rate [21] and serves as a source. The $\mathbf{E} \cdot \mathbf{B}$ term governs the coupling between the chiral density and the electromagnetic field: twisting or untwisting magnetic field lines alters the net chirality in the system, acting as either a source or a sink depending on its sign.

Equation (4) should be viewed alongside the time evolution of the magnetic helicity, which takes the form [12, 22]:

$$\frac{\partial(\mathbf{A} \cdot \mathbf{B})}{\partial t} = -2c\mathbf{E} \cdot \mathbf{B} - c\nabla \cdot (\mathbf{E} \times \mathbf{A}), \quad (5)$$

The two equations, when combined and integrated over a volume, yield a generalized helicity balance law:

$$\frac{d}{dt} \left(Q_5 + \frac{\alpha}{\pi\hbar c} \chi_m \right) + \Gamma_5 = 0. \quad (6)$$

Here, $Q_5 = \int n_5 dV$ is the total axial charge, $\chi_m = \int \mathbf{A} \cdot \mathbf{B} dV$ is the total magnetic helicity, and $\Gamma_5 = \int n_5 \Gamma_f dV$ is the average spin-flip rate. Total helicity is not strictly conserved due to the sink term Γ_5 . We neglect the helicity flux across the boundary ($\propto \mathbf{E} \times \mathbf{A}$) and the weak interaction processes ($\Gamma_w^{\text{eff}} \ll \Gamma_f$), both of which contribute marginally. Nonetheless, weak interactions may enhance the effect if the NS is out of chemical equilibrium. For simplicity, we set $\Gamma_w^{\text{eff}} = 0$ hereafter.

Concerning the spin-flip reaction rate, electrons interact via Rutherford, electron-electron, or Compton scattering. In the core, Rutherford scattering dominates [11, 23], while in the crust, electron-nucleus scattering prevails. For degenerate electrons, the flip rate is given by [24]:

$$\Gamma_f = \frac{4\alpha}{3\pi\sigma_e} \frac{m_e^2 c^4}{\hbar^2}, \quad (7)$$

Since σ_e depends on temperature, so does Γ_f , underscoring the need to consider the coupled evolution of temperature and magnetic field in simulations.

Given that all reaction rates are much faster than typical astrophysical timescales, we treat all quantities in Equation (4), except the chiral density n_5 , as constant in time to derive an analytical solution:

$$n_5(t) = \left(\frac{2\alpha}{\pi\hbar} \frac{\mathbf{E} \cdot \mathbf{B}}{\Gamma_f} \right) (1 - e^{-\Gamma_f t}) + n_5^0 e^{-\Gamma_f t}. \quad (8)$$

where n_5^0 is the initial chiral number density. On astrophysical timescales ($t \gg \Gamma_f^{-1}$), the system reaches a quasi-equilibrium state:

$$n_5(t) \approx \frac{2\alpha}{\pi\hbar} \frac{\mathbf{E} \cdot \mathbf{B}}{\Gamma_f} \quad (9)$$

The chiral chemical potential μ_5 is related to the chiral number density n_5 via the standard expression $n_5 = \mu_e^2 \mu_5 / (\pi^2 (\hbar c)^3)$, valid in the regime of highly degenerate NS matter where $\mu_e \gg T$. Substituting the expression for $\mathbf{E} \cdot \mathbf{B}$ into Equation (9), we obtain an explicit expression for k_5 :

$$k_5(\mathbf{x}, t) = \frac{(\nabla \times \mathbf{B}) \cdot \mathbf{B}}{\frac{\mu_e^2}{8\pi\alpha^2\eta(\hbar c)} \Gamma_f + B^2} = \frac{(\nabla \times \mathbf{B}) \cdot \mathbf{B}}{\left(\frac{2\mu_e^2}{m_e^2 c^4} \right) \frac{B_{\text{QED}}^2}{3\pi} + B^2}, \quad (10)$$

and $B_{\text{QED}} \equiv m_e^2 c^3 / (e\hbar) = 4.41 \times 10^{13}$ G is the Schwinger QED critical field.

Equation (10) highlights the two main contributions to the chiral asymmetry: the numerator originates from magnetic helicity and increases when $\nabla \times \mathbf{B}$ aligns with \mathbf{B} . This alignment characterizes the so-called *helical*

magnetic fields, where toroidal and poloidal components reinforce each other. In contrast, the spin-flip term in the denominator suppresses chiral asymmetry. If the magnetic field configuration possesses a non-zero average magnetic helicity, a small but appreciable chiral asymmetry can be sustained despite the action of spin-flip processes.

We define the characteristic wavenumber associated with the magnetic field as

$$k_B \equiv \frac{(\nabla \times \mathbf{B}) \cdot \mathbf{B}}{B^2}. \quad (11)$$

In the weak-field regime ($B \ll B_{\text{QED}}$), we find $k_5 \propto k_B B^2 / B_{\text{QED}}^2 \ll k_B$. In contrast, in the strong-field regime ($B > B_{\text{QED}}$) $k_5 \lesssim k_B$. Thus, the scale k_5 is ultimately bounded by the characteristic wavenumber of the background magnetic field.

To estimate the characteristic magnetic field strength at which saturation sets in, we equate the two terms in the denominator of Equation (10). This condition is satisfied when:

$$B_{\text{sat}} \approx \sqrt{\frac{2}{3\pi}} \frac{\mu_e}{m_e c^2} B_{\text{QED}}. \quad (12)$$

The saturation field B_{sat} scales linearly with the ratio $\mu_e / (m_e c^2)$, which increases with density. Under typical NS conditions, this ratio ranges from 10 in the outer crust to 200 in the inner crust, yielding $B_{\text{sat}} \sim 10^{14}$ G near the surface and up to $\sim 5 \times 10^{15}$ G in deeper layers—consistent with inferred magnetar field strengths.

It is insightful to explicitly write the conservation equations for electromagnetic energy and the additional electron energy from chiral imbalance (see [15] for a thorough discussion on energy conservation):

$$\begin{aligned} \frac{d\varepsilon_{em}}{dt} &= -\sigma_e \mathbf{E}^2 - \frac{\alpha\mu_5}{\pi\hbar} \mathbf{E} \cdot \mathbf{B} - \frac{c}{4\pi} \nabla \cdot (\mathbf{E} \times \mathbf{B}), \\ \frac{d\varepsilon_5}{dt} &= -\frac{1}{2} \mu_5 n_5 \Gamma_f + \frac{\alpha\mu_5}{\pi\hbar} \mathbf{E} \cdot \mathbf{B}. \end{aligned} \quad (13)$$

Here, each term on the right-hand side plays a distinct role. The first term in both equations represents a sink: Joule dissipation for magnetic energy and spin-flip processes for chiral energy. The final term in the magnetic energy equation corresponds to the Poynting flux, which becomes a surface term upon volume integration. The $\mathbf{E} \cdot \mathbf{B}$ terms describe the conservative exchange of energy between the magnetic field and chirality.

Integrating over the stellar volume, the total energy balance reads:

$$\frac{d}{dt} (E_{em} + E_5) + S_{\text{tot}} + Q_{\text{tot}} + \Gamma_{5\text{tot}} = 0, \quad (14)$$

where $S_{\text{tot}} = \frac{c}{4\pi} \oint dS \cdot (\mathbf{E} \times \mathbf{B})$ is the total Poynting flux, $\Gamma_{5\text{tot}} = \frac{1}{2} \int \mu_5 n_5 \Gamma_f dV$ is the total spin-flip dissipation rate, and Q_{tot} is the total Joule dissipation, given by:

$$Q_{\text{tot}} = \int \sigma_e \mathbf{E}^2 dV. \quad (15)$$

In the absence of the Hall drift term, $c\mathbf{E} = \eta(\nabla \times \mathbf{B} - k_5 \mathbf{B})$, and the chiral correction can offset magnetic dissipation if $\nabla \times \mathbf{B} \approx k_5 \mathbf{B}$.

To assess the impact of the CME on magnetic field evolution in NSs, we performed magneto-thermal simulations using an extended 3D finite-volume version of the MATINS code [25–27]. This version solves the coupled induction and heat diffusion equations, consistently incorporating chiral and spin-flip terms arising from the chiral anomaly. To focus on the NS crust, we apply potential-field boundary conditions (current-free magnetosphere) at an outer numerical boundary located at $\rho = 10^{10} \text{ g cm}^{-3}$, near the transition between the liquid envelope and the solid crust. At the crust–core interface, we impose perfect-conductor boundary conditions. The temperature-dependent electrical conductivity is computed at each point of the star using the codes from the IOFFE repository² [28]. In MATINS, the NS background model can be constructed using various zero-temperature equation of states (EOSs) from the CompOSE online database³. For this study, we adopt the BSk24 EOS [29], assuming a canonical NS with mass $M = 1.4 M_\odot$, radius $R = 12.4$ km, and crustal thickness of 0.86 km.

Magnetic helicity plays a central role in magnetic field dynamics [30], enabling inverse cascades that transfer energy from small to large scales. In NS crusts, such cascades are typically driven by the Hall effect on Hall timescales [31, 32]. However, Dehman & Brandenburg [32] showed that, although present, this process fails to significantly amplify the large-scale dipolar field due to the crust’s extreme radial-to-angular aspect ratio. To isolate and better assess the role of chirality, we deliberately disable the nonlinear Hall term and focus solely on the impact of the CME.

As detailed in Section II, we initialize our simulations with a turbulent magnetic field concentrated at small scales, with an average strength of $\sim 10^{16}$ G [6, 33]. The field is initially divided between poloidal and toroidal components, with a dominant toroidal contribution, consistent with the small-scale energy spectra predicted by proto-NS dynamo simulations [6]. We limit the dipolar component to a few 10^{12} G, much weaker than the large-scale fields inferred observationally for magnetars. The total magnetic energy, of order a few 10^{49} erg, remains small compared to the star’s gravitational binding energy ($\sim 10^{53}$ erg) or the rotational energy of a millisecond pulsar ($\sim 10^{51-52}$ erg).

The magnetic energy spectrum peaks at $\ell_0 \approx 50$, extends up to $\ell_{\text{max}} = 70$, and follows a ℓ^4 slope. We consider three initial setups: (i) Full Slope (Run F), preserving the full ℓ^4 spectrum and naturally concentrating energy near ℓ_0 ; (ii) Damped (Run D), where the magnetic energy is attenuated by roughly two orders of mag-

² <http://www.ioffe.ru/astro/conduct/>

³ <https://compose.obspm.fr/>

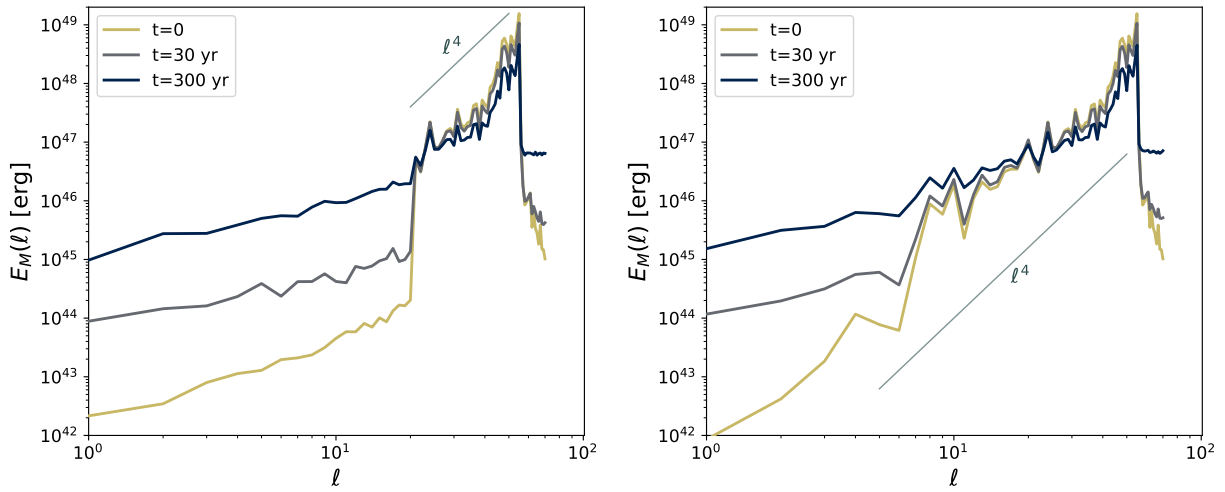


FIG. 1. Magnetic energy spectra for Run D (left) and Run F (right) as a function of multipole degree ℓ . Spectra are shown at $t = 0$ (yellow), $t = 30$ yr (dark gray), and $t = 300$ yr (dark blue), with a reference ℓ^4 slope overplotted in light gray.

nitude for $\ell = 1 \dots 20$, concentrating the remaining energy between $\ell = 21$ and ℓ_0 ; and (iii) Damped–No CME (Run DO), a replica of Run D without CME. The radial wavenumber is set to $k_r \approx 400 \text{ km}^{-1}$ (Figure 3), balancing the fastest-growing CME modes – characterized by chiral wavelengths of a few meters – against Ohmic dissipation. To resolve these small scales, we adopt $N_r = 200$ radial points, reflecting the CME’s strong sensitivity to microphysical properties (e.g., η and μ_e), which vary primarily with radius. Angular directions are discretized using a cubed-sphere grid [25], with $N_\xi = N_\eta = 47$ points per patch across six patches, yielding $N_\theta = 94$ and $N_\phi = 188$ grid points, and resolving angular structures down to a few hundred meters. Starting from these initial conditions, we run three global NS crust simulations, evolving each over the first few hundred years with a timestep of days—consistent with the ages of the youngest magnetars, such as Swift J1818.0–1607 (~ 200 yr; [34]).

In the absence of spin-flip processes (an unphysical case), the axial charge Q_5 would grow to match the initial magnetic helicity ($\frac{\alpha}{\pi \hbar c} \chi_m$), conserving total helicity. However, spin-flip scattering restores chiral balance, suppressing Q_5 by nearly 20 orders of magnitude, leaving a tiny residual – sufficient to drive chiral-induced magnetic field evolution. See Section III in the Supplemental Material for details.

To assess the impact of this residual asymmetry, Figure 1 shows the total magnetic energy spectra for Run D (left) and Run F (right) at $t = 0$, $t = 30$ yr, and $t = 300$ yr. A significant energy transfer—about two orders of magnitude—occurs toward multipoles with initially weak fields ($\ell \leq 20$), as the emergence of a nonzero k_5 enables the CME to redistribute magnetic energy across spatial scales, boosting weaker regions at the expense of stronger ones. A particularly striking feature is the strong amplification of the dipolar component ($\ell = 1$), marking the nat-

ural formation of the largest and hardest-to-form scale. In Run D, the initial slope (nearly linear in ℓ) at $\ell \leq 20$ is preserved but amplified, whereas in Run F, the slope at large-scales evolves toward an approximately linear dependence on ℓ , leading to comparable magnetic energy spectra in both runs. In both cases, the CME preserves the spectral peak at ℓ_0 , which – being at small scales – is more susceptible to Ohmic dissipation over tens of kiloyears. By contrast, an inverse cascade typically shifts the peak toward lower ℓ , enhancing the longevity of the large-scale field [31].

While this process may resemble an inverse cascade, its underlying mechanism is fundamentally different. In the presence of a helical magnetic field (as in our configuration) and an active Hall term, an inverse cascade can occur, though its impact is typically much weaker [32]. In such cases, nonlinear interactions, as shown by Frisch [35], transfer energy and helicity to larger scales through mode couplings that satisfy $\mathbf{k} = \mathbf{p} + \mathbf{q}$ with $|\mathbf{k}| \leq \max(|\mathbf{p}|, |\mathbf{q}|)$. By contrast, the CME operates simultaneously on all multipoles, enabling the redistribution of magnetic energy from small to larger scales in our simulations.

Figure 2 illustrates the decay of the average magnetic field (mauve, left axis) alongside the growth of the dipolar field (black, right axis). Note the different scales on the left and right vertical axes. Run F, Run D, and Run DO are represented with solid, dash-dotted, and dotted lines, respectively.

As expected, the average magnetic field decreases over time in all three runs. For reference, we show with dots Run DO including only Ohmic dissipation. We observe a rapid decay of the initial small-scale magnetic field following $\propto \exp(-t/\tau_{\text{Ohm}})$, with $\tau_{\text{Ohm}} \equiv 1/\eta k^2 \approx 20 \dots 25$ yr. The initially weak dipolar field also undergoes decay, though at a slower rate due to its smaller wavenumber k .

In contrast, the CME is active in Runs F and D, trans-

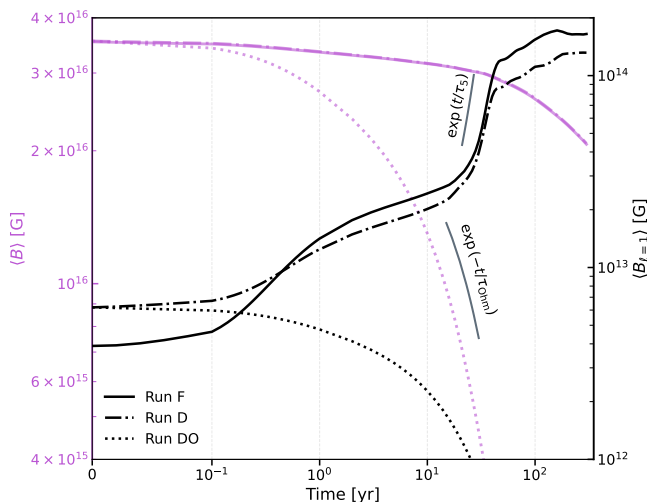


FIG. 2. Time evolution of the average magnetic field (mauve, left axis; scaling from 4×10^{15} G to 4×10^{16} G) and dipolar field (black, right axis; scaling from 10^{12} G to 2×10^{14} G). Solid lines correspond to Run F, dash-dotted lines to Run D, and dotted lines to Run DO. Gray lines show fits to the growth and decay phases, with $\tau_{\text{Ohm}} \equiv 1/\eta k^2 \approx 20 \dots 25$ yr and $\tau_5 \equiv 1/\eta k k_5 \approx 5 \dots 10$ yr.

ferring a portion of the energy from the small-scale initial magnetic field to the dipolar component, which consequently grows over time. It is worth noting that overall dissipation is significantly slower than in Run DO, as the self-regulating chiral current effectively counteracts much of the original electric current along the magnetic field lines, thereby reducing the net Joule dissipation rate (Eq. (15)).

In Runs F and D, we identify three distinct stages in the growth of the dipolar components. During the initial few months ($t \leq 0.1$ yr), little noticeable difference appears, as the chiral asymmetry is still developing from the initial turbulent average field. This is followed by a gradual growth phase lasting 20 to 30 years, and then by a second, exponential growth phase spanning several decades. We interpret this latter phase as a manifestation of the chiral magnetic instability (CMI), with the growth approximately following $\propto \exp(t/\tau_5)$, with $\tau_5 \equiv 1/\eta k k_5 \approx 5 \dots 10$ yr. As expected, the growth saturates at $B \gtrsim 10^{14}$ G after ~ 100 yr, consistent with magnetar observations. For a detailed analysis of the magnetic field evolution in Run F, see Section III of the Supplemental Material.

Our research reveals that magnetic helicity, a classical attribute, triggers a subtle chiral asymmetry—a quantum anomaly—in macroscopic astrophysical bodies like NSs. This faint chirality significantly shapes magnetic field evolution over centuries, overcoming robust spin-flip suppression. The CME restructures the magnetic field spectrum by redistributing energy across scales, converging toward a nearly linear slope in multipole degree ℓ , particularly for $\ell < 10$, which governs large-scale astro-

physical observables.

An initial intense (10^{16} G) very small-scale field naturally evolves into a mixed poloidal/toroidal dipolar field, amplified to 10^{14} G—consistent with observed magnetar strengths. Although small-scale fields initially persist after this short stage (lasting 100 years), they are more prone to Ohmic decay and will dissipated in a few thousand years. This strong small-scale field may potentially drive the high X-ray luminosities ($L_X \gtrsim 10^{35}$ erg/s) and burst activity, due to energy stored at small scales [36]. Conversely, the large-scale dipolar field decays more gradually, persisting as a long-lived feature. This interaction between magnetic helicity and the chiral anomaly establishes a novel framework for understanding magnetar field evolution.

A key insight from our study is the geometry of the resulting magnetic field. Previous research [25, 26, 36–40] on long-term magneto-thermal evolution indicate that crust-confined fields with prominent large-scale structures align best with observational data. However, generating such configurations is difficult, as conventional proto-NS dynamo processes create intense small-scale turbulence but struggle to produce crust-confined large-scale dipolar fields. Our work introduces a mechanism that naturally achieves this geometry. We have presented the first self-consistent, long-term simulations of the CME-driven magnetic evolution, establishing this mechanism as a key ingredient for magnetar dynamics.

Enhancing numerical resolution at small scales is anticipated to amplify the observed effects further, and we plan to refine this in future simulations. This study specifically isolates the CME under strong magnetic fields by deliberately excluding the nonlinear Hall term, enabling a clear analysis of the CME role. A future investigation will explore the impact of the Hall effect on the chiral anomaly. Preliminary results suggest that the Hall effect has a limited influence on the early-time (100 years) evolution, the focus of this paper, as it generally operates over longer timescales.

ACKNOWLEDGMENTS

We gratefully acknowledge the generous hospitality and stimulating discussions with Sanjay Reddy and the participants of the programs “*IReNA-INT Joint Workshop on Thermal and Magnetic Evolution of Neutron Stars*” at the University of Washington, Seattle, and “*Breaking New Ground in Supernova Physics 2025: Crossroads of Turbulence, Chiral Dynamics, and Machine Learning*” at Fukuoka University, Japan. CD acknowledges support from the Ministerio de Ciencia, Innovación y Universidades, co-funded by the Agencia Estatal de Investigación, the Unión Europea (FSE+), and the Universidad de Alicante. Her contract is part of the fellowship JDC2023-052227-I, funded by MCIU/AEI/10.13039/501100011033 and the FSE+. We also acknowledge support from the Conselleria

d'Educació, Cultura, Universitats i Ocupació de la Generalitat Valenciana, through grant CIPROM/2022/13,

and from the AEI grant PID2021-127495NB-I00 funded by MCIN/AEI/10.13039/501100011033.

-
- [1] S. Mereghetti, J. A. Pons, and A. Melatos, *Space Sci. Rev.*, **191**, 315 (2015), arXiv:1503.06313 [astro-ph.HE].
- [2] P. Esposito, N. Rea, and G. L. Israel, in *Timing Neutron Stars: Pulsations, Oscillations and Explosions*, Astrophysics and Space Science Library, Vol. 461, edited by T. M. Belloni, M. Méndez, and C. Zhang (2021) pp. 97–142, arXiv:1803.05716 [astro-ph.HE].
- [3] S. A. Balbus and J. F. Hawley, *Astrophys. J.* **376**, 214 (1991).
- [4] M. Obergaulinger, H. T. Janka, and M. A. Aloy, *MNRAS* **445**, 3169 (2014), arXiv:1405.7466 [astro-ph.SR].
- [5] R. Raynaud, J. Guilet, H.-T. Janka, and T. Gastine, *Science Advances* **6**, eaay2732 (2020), arXiv:2003.06662 [astro-ph.HE].
- [6] A. Reboul-Salze, J. Guilet, R. Raynaud, and M. Bugli, *A&A* **645**, A109 (2021), arXiv:2005.03567 [astro-ph.HE].
- [7] M. Á. Aloy and M. Obergaulinger, *MNRAS* **500**, 4365 (2021), arXiv:2008.03779 [astro-ph.HE].
- [8] Y. Masada, K. Kotake, T. Takiwaki, and N. Yamamoto, *Phys. Rev. D* **98**, 083018 (2018), arXiv:1805.10419 [astro-ph.HE].
- [9] J. Matsumoto, N. Yamamoto, and D.-L. Yang, *prd* **105**, 123029 (2022), arXiv:2202.09205 [astro-ph.HE].
- [10] D. Grabowska, D. B. Kaplan, and S. Reddy, *prd* **91**, 085035 (2015), arXiv:1409.3602 [hep-ph].
- [11] G. Sigl and N. Leite, *jcap* **2016**, 025 (2016), arXiv:1507.04983 [astro-ph.HE].
- [12] A. Boyarsky, J. Fröhlich, and O. Ruchayskiy, *Phys. Rev. Lett.* **108**, 031301 (2012), arXiv:1109.3350 [astro-ph.CO].
- [13] H. Tashiro, T. Vachaspati, and A. Vilenkin, *Phys. Rev. D* **86**, 105033 (2012), arXiv:1206.5549 [astro-ph.CO].
- [14] P. Pavlović, N. Leite, and G. Sigl, *Phys. Rev. D* **96**, 023504 (2017), arXiv:1612.07382 [astro-ph.CO].
- [15] D. B. Kaplan, S. Reddy, and S. Sen, *prd* **96**, 016008 (2017), arXiv:1612.00032 [hep-ph].
- [16] S. L. Adler, *Physical Review* **177**, 2426 (1969).
- [17] J. S. Bell and R. Jackiw, *Nuovo Cimento A Serie* **60**, 47 (1969).
- [18] A. Vilenkin, *Phys. Rev. D* **22**, 3080 (1980).
- [19] J. A. Pons and D. Viganò, *Living Reviews in Computational Astrophysics* **5**, 3 (2019), arXiv:1911.03095 [astro-ph.HE].
- [20] I. Rogachevskii, O. Ruchayskiy, A. Boyarsky, J. Fröhlich, N. Kleeorin, A. Brandenburg, and J. Schober, *apj* **846**, 153 (2017), arXiv:1705.00378 [physics.plasm-ph].
- [21] R. I. Epstein and C. J. Pethick, *Astrophys. J.* **243**, 1003 (1981).
- [22] D. Biskamp, *Nonlinear Magnetohydrodynamics*, Cambridge Monographs on Plasma Physics (Cambridge University Press, 1997).
- [23] M. Dvornikov and V. B. Semikoz, *prd* **92**, 083007 (2015), arXiv:1507.03948 [astro-ph.HE].
- [24] P. Haensel, A. Y. Potekhin, and D. G. Yakovlev, *Neutron stars 1: Equation of state and structure*, Astrophysics and Space Science Library, Vol. 326 (Springer, New York, USA, 2007).
- [25] C. Dehman, D. Viganò, J. A. Pons, and N. Rea, *MNRAS* **518**, 1222 (2023), arXiv:2209.12920 [astro-ph.HE].
- [26] C. Dehman, D. Viganò, S. Ascenzi, J. A. Pons, and N. Rea, *MNRAS* **523**, 5198 (2023), arXiv:2305.06342 [astro-ph.HE].
- [27] S. Ascenzi, D. Viganò, C. Dehman, J. A. Pons, N. Rea, and R. Perna, *arXiv e-prints*, arXiv:2401.15711 (2024), arXiv:2401.15711 [astro-ph.HE].
- [28] A. Y. Potekhin, J. A. Pons, and D. Page, *Space Science Reviews* **191**, 239 (2015).
- [29] J. M. Pearson, N. Chamel, A. Y. Potekhin, A. F. Fantina, C. Ducoin, A. K. Dutta, and S. Goriely, *Monthly Notices of the Royal Astronomical Society* **481**, 2994 (2018), <https://academic.oup.com/mnras/article-pdf/481/3/2994/25817956/sty2413.pdf>.
- [30] A. Brandenburg, in *Cosmic Magnetic Fields*, Vol. 664, edited by R. Wielebinski and R. Beck (2005) p. 219.
- [31] A. Brandenburg, *Astrophys. J.* **901**, 18 (2020), arXiv:2006.12984 [astro-ph.HE].
- [32] C. Dehman and A. Brandenburg, *A&A* **694**, A39 (2025), arXiv:2408.08819 [astro-ph.HE].
- [33] Y. Masada, T. Takiwaki, and K. Kotake, *Astrophys. J.* **924**, 75 (2022), arXiv:2001.08452 [astro-ph.HE].
- [34] P. Esposito, N. Rea, A. Borghese, F. C. Zelati, D. Viganò, G. L. Israel, A. Tiengo, A. Ridolfi, A. Possenti, M. Burgay, D. Götz, F. Pintore, L. Stella, C. Dehman, M. Ronchi, S. Campana, A. Garcia-Garcia, V. Graber, S. Mereghetti, R. Perna, G. A. R. Castillo, R. Turolla, and S. Zane, *The Astrophysical Journal Letters* **896**, L30 (2020).
- [35] U. Frisch, A. Pouquet, J. Leorat, and A. Mazure, *JFM* **68**, 769 (1975).
- [36] C. Dehman, D. Viganò, N. Rea, J. A. Pons, R. Perna, and A. Garcia-Garcia, *ApJL*, **902**, L32 (2020), arXiv:2010.00617 [astro-ph.HE].
- [37] U. Geppert, J. Gil, G. Melikidze, J. Pons, and D. Viganò, in *Electromagnetic Radiation from Pulsars and Magnetars*, Astronomical Society of the Pacific Conference Series, Vol. 466, edited by W. Lewandowski, O. Maron, and J. Kijak (2012) p. 187, arXiv:1206.1790 [astro-ph.SR].
- [38] D. Viganò, N. Rea, J. A. Pons, R. Perna, D. N. Aguilera, and J. A. Miralles, *MNRAS* **434**, 123 (2013), arXiv:1306.2156 [astro-ph.SR].
- [39] K. N. Gourgouliatos and J. A. Pons, *Physical Review Research* **1**, 032049 (2019).
- [40] D. De Grandis, R. Taverna, R. Turolla, A. Gnani, S. B. Popov, S. Zane, and T. S. Wood, *Astrophys. J.* **914**, 118 (2021), arXiv:2105.00684 [astro-ph.HE].
- [41] S. Chandrasekhar and P. C. Kendall, *Astrophys. J.* **126**, 457 (1957).
- [42] U. Geppert and H. J. Wiebicke, *A&A* **87**, 217 (1991).
- [43] F. Krause and K.-H. Rädler, *Oxford: Pergamon Press, 1980* (Pergamon Press, Oxford, 1980).
- [44] D. N. Aguilera, J. A. Pons, and J. A. Miralles, *A&A* **486**, 255 (2008), arXiv:0710.0854 [astro-ph].
- [45] R. Durrer and C. Caprini, *JCAP* **2003**, 010 (2003).

Supplemental Material

In the following sections, we first decompose the induction equation (excluding the Hall term) into its poloidal and toroidal magnetic field components to demonstrate how the chiral current induces coupling between them (Section I). We then describe the setup of the initial magnetic field used in this study (Section II), followed by an extended analysis of our simulation results (Section III).

I. SIMPLIFIED DISCUSSION OF THE CME IN THE INDUCTION EQUATION

The magnetic field can be decomposed into poloidal (\mathbf{B}_p) and toroidal (\mathbf{B}_t) components as follows [41]:

$$\mathbf{B} = \mathbf{B}_p + \mathbf{B}_t, \quad (16)$$

$$\mathbf{B}_t = -\mathbf{r} \times \nabla \Psi, \quad \mathbf{A}_t = -\mathbf{r} \times \nabla \Phi, \quad \mathbf{B}_p = \nabla \times \mathbf{A}_t = -\mathbf{r} \Delta \Phi + \nabla \frac{\partial}{\partial r} (r \Phi), \quad (17)$$

where \mathbf{A}_t is the toroidal vector potential. The two scalar functions $\Phi(\mathbf{r}, t)$ and $\Psi(\mathbf{r}, t)$ uniquely define the poloidal and toroidal components, respectively.

The induction equation (Eq. (2)) can also be decomposed into poloidal and toroidal parts. Neglecting the Hall term and retaining only the Ohmic and chiral contributions, one can follow the same methodology as in Geppert & Wiebicke [42] to obtain

$$\begin{aligned} \frac{\partial \Phi}{\partial t} &= \eta (\Delta \Phi + k_5 \Psi), \\ \frac{\partial \Psi}{\partial t} &= \eta (\Delta \Psi - k_5 \Delta \Phi). \end{aligned} \quad (18)$$

The additional term proportional to k_5 accounts for the CME. For clarity, we have omitted the spatial (radial and angular) dependence of the magnetic diffusivity η and the chiral wavenumber k_5 , and assumed they are constants.

Next, we expand the scalar functions in spherical harmonics [43]:

$$\begin{aligned} \Phi(t, r, \theta, \phi) &= \frac{1}{r} \sum_{\ell m} \Phi_{\ell m}(r, t) Y_{\ell m}(\theta, \phi), \\ \Psi(t, r, \theta, \phi) &= \frac{1}{r} \sum_{\ell m} \Psi_{\ell m}(r, t) Y_{\ell m}(\theta, \phi), \end{aligned} \quad (19)$$

where $\ell = 1, 2, \dots$ denotes the multipole degree and $m = -\ell, \dots, \ell$ the azimuthal order. Equation (18) yields a set of equations that couples the toroidal and poloidal components of each multipole, taking the following form:

$$\begin{aligned} \frac{\partial \Phi_{\ell m}}{\partial t} &= \eta \Delta \Phi_{\ell m} + \eta k_5 \Psi_{\ell m}, \\ \frac{\partial \Psi_{\ell m}}{\partial t} &= \eta \Delta \Psi_{\ell m} - \eta k_5 \Delta \Phi_{\ell m}, \end{aligned} \quad (20)$$

where

$$\Delta \equiv \left(\frac{\partial^2}{\partial r^2} - \frac{\ell(\ell+1)}{r^2} \right). \quad (21)$$

Note that incorporating the spatial dependence of η and k_5 would introduce additional coupling terms in the equations. In this form, the role of k_5 becomes evident. First, it couples independently to all multipoles (ℓ, m) of the toroidal and poloidal components. Second, the evolution equations show that an initial poloidal (or toroidal) field acts as a source in the toroidal (or poloidal) evolution equation, naturally generating its complementary counterpart and driving the system toward an approximate equipartition of magnetic energy between the two. However, this coupling is inherently asymmetric: the poloidal field couples directly to the toroidal magnetic component, while the toroidal field couples to the toroidal current (i.e., the curl of the poloidal component).

To simplify the discussion, we introduce additional notation. The Laplacian operator acts on each mode as

$$\Delta \rightarrow -(k_r^2 + k_{ang}^2), \quad (22)$$

where k_r characterizes the radial dependence (i.e., $\partial/\partial r \rightarrow ik_r$), and the angular wavenumber is $k_{\text{ang}} = \sqrt{\ell(\ell+1)}/r$, reducing the equations to:

$$\begin{aligned}\frac{\partial \Phi_{\ell m}}{\partial t} &= -\eta (k^2 \Phi_{\ell m} - k_5 \Psi_{\ell m}), \\ \frac{\partial \Psi_{\ell m}}{\partial t} &= -\eta (k^2 \Psi_{\ell m} - k_5 k^2 \Phi_{\ell m}).\end{aligned}\quad (23)$$

Consider a field satisfying the condition $\Psi_{\ell m} = k \Phi_{\ell m}$. The equations then become

$$\begin{aligned}\frac{\partial \Phi_{\ell m}}{\partial t} &= -\eta k(k - k_5) \Phi_{\ell m}, \\ \frac{\partial \Psi_{\ell m}}{\partial t} &= -\eta k(k - k_5) \Psi_{\ell m},\end{aligned}\quad (24)$$

which admit exponentially growing or damped modes, depending on the sign of $k - k_5$. For $k > k_5$, the instability is suppressed by Ohmic dissipation (if k_5 is negative, dissipation is even enhanced). In contrast, for $k < k_5$, the CMI develops, and the fastest-growing chiral modes ($k \approx k_5/2$) dominate. These fastest-growing chiral modes are associated with small-scale magnetic structures (typically ranging from centimeters to meters), characterized by the CME wavelength:

$$\lambda \equiv \frac{\pi}{k_5} = \frac{\pi \hbar c}{4\alpha \mu_5}. \quad (25)$$

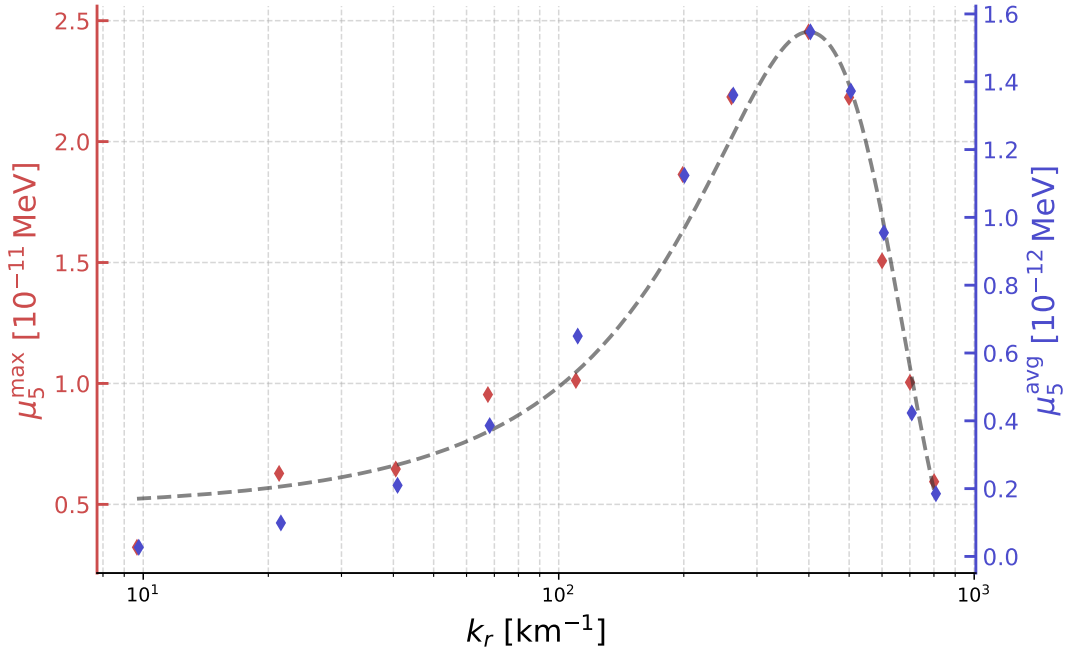


FIG. 3. Maximum (μ_5^{max} in units of 10^{-11} MeV; red diamonds) and average (μ_5^{avg} in units of 10^{-12} MeV; blue diamonds) chiral chemical potentials as functions of the radial wavenumber k_r , computed at the initial time for an average magnetic field of a few 10^{16} and a temperature of $T = 10^9$ K. The peak occurs at $k_0 \approx 400$ km^{-1} , corresponding to a wavelength $\lambda \approx 14$ m. The gray dashed curve shows an asymmetric Gaussian fit, $\mu_5^{\text{max}}(k_r) = \mu_5^0 \exp[-(k_r - k_0)^2/(2\sigma_{\pm}^2)]$, with different widths σ_- and σ_+ on either side of the peak. Here, $\mu_5^0 \equiv \mu_5^{\text{max}}(k_0) \approx 2.5 \times 10^{-11}$ MeV.

II. INITIAL MAGNETIC FIELD STRUCTURE AND OPTIMAL CME MODE

All the microphysical properties relevant for the CME in the NS interior (e.g., magnetic diffusivity η , electron chemical potential μ_e), vary rapidly in the radial direction, and to a lesser extent in angular directions due to possible

temperature anisotropies. Since the crust is very thin compared to the star's perimeter, radial gradients are expected to dominate the dynamics. This highlights the need for higher radial resolutions in the simulations. Thus, one can expect $k_r \gg k_{ang}$, and we can approximate $k^2 \approx k_r^2$.

Guided by this insight, we construct the initial magnetic field in the NS crust using MATINS by prescribing the angular and radial profiles of the scalar functions $\Phi(\mathbf{r}, t=0)$ and $\Psi(\mathbf{r}, t=0)$ (see Eq. (19)).

The radial function $\Phi_{\ell m}$ takes the following form [44]:

$$\Phi_{\ell m}(r) = \Phi_{\ell m}^0 k_r r (a + \tan(k_r R) b), \quad (26)$$

where a and b are chosen to satisfy the inner and outer boundary conditions [44], and $\Phi_{\ell m}^0$ are normalization factors evaluated at a reference radius, just beneath the stellar surface R_* . These weights are chosen to concentrate magnetic energy at small angular scales, following a spectral slope proportional to ℓ^4 in the sub-inertial range ($\ell < \ell_0$), where ℓ_0 denotes the spectral peak [45].

We encode magnetic helicity by directly relating the toroidal scalar function via:

$$\Psi_{\ell m}(r) = \alpha_{\ell m} \Phi_{\ell m}(r), \quad (27)$$

where, being conservative, we set $\alpha_{\ell m} = \sqrt{\ell(\ell+1)}/R$, where R is the radius at the surface of our computational domain. For a maximally helical field, one should choose $\alpha_{\ell m} = k$.

Employing curl operators adapted to cubed-sphere coordinates [25], we derive the magnetic field components from these scalar functions using Equation (17). This method guarantees an initial magnetic field that is divergence-free (to machine precision), free of axis singularities, and intrinsically helical—a key property for investigating CME-driven magnetic evolution.

The radial direction in the crust is resolved with 200 grid points, capturing structures down to a few meters. Angular directions are discretized using a cubed-sphere grid [25], with $N_\xi = N_\eta = 47$ points per patch across six patches, yielding $N_\theta = 94$ and $N_\phi = 188$ grid points, and resolving multipoles up to $\ell_{\max} \sim 70$, corresponding to angular scales of a few hundred meters. With this setup, we vary the radial wavenumber k_r while keeping the initial average magnetic field and temperature fixed. For each configuration, we compute the predicted average (μ_5^{avg}) and maximum (μ_5^{max}) values of the initial chiral chemical potential $\mu_5(\mathbf{x})$.

Figure 3 summarizes the results: maximum (red diamonds) and average (blue diamonds) values of μ_5 as functions of k_r , evaluated for a mean magnetic field of a few 10^{16} G concentrated at small scales and a temperature of 10^9 K—typical of young magnetars. The optimal radial wavenumber is found at $k_0 \approx 400 \text{ km}^{-1}$, corresponding to a wavelength $\lambda_0 \approx 14$ m, and we ensure that this scale is resolved by our radial grid. Notably, the values of μ_5 are many orders of magnitude smaller than the electron chemical potential ($\mu_e \approx 10 \dots 100$ MeV), yet they lead to significant changes in the field evolution.

III. DETAILED ANALYSIS OF MAGNETIC FIELD EVOLUTION

In this section, we present an extended analysis of Run F. We examine the growth of the dipolar magnetic field, the decay of the mean magnetic field, and the energy transfer between poloidal and toroidal components. We also assess the conservation of total helicity and energy, as outlined in our theoretical framework.

Figure 4 shows the time evolution of the average magnetic field (left panel) and the dipolar magnetic field (right panel) for Run F. The toroidal (dash-double-dot) and poloidal (dotted) contributions are also shown. In contrast to Figure 2 in the main text, this figure highlights the interplay between the toroidal and poloidal components. Three distinct stages are observed in the decay of the total magnetic field and the growth of the dipolar field: i) Early stage ($t \lesssim 0.1$ yr): Both the total and dipolar magnetic fields remain nearly constant. This reflects the initial buildup of the CME, during which the chiral asymmetry is still developing and its dynamical effects are negligible. ii) Intermediate stage (up to ~ 30 yr): A modest decline in the total magnetic field begins, primarily due to the dissipation of the dominant toroidal component. During this stage, the CME becomes active, transferring energy from the toroidal field to the initially subdominant poloidal field. At the same time, we observe in the right panel the simultaneous growth of both components of the dipolar field. Energy is continuously exchanged between them, maintaining an approximate equipartition. iii) Late stage (beyond ~ 30 yr): At this point, the growth of the poloidal component in the total field halts. Both components have reached similar strengths and begin to dissipate at comparable rates. Meanwhile, the dipolar field exhibits exponential growth, $\propto \exp(t/\tau_5)$, with $\tau_5 \approx 5 \dots 10$ years—signaling the onset of the CMI. During this process, both components of the dipolar field reach 10^{14} G. After about a hundred years, the growth saturates.

For completeness, Figure 5 shows the generalized helicity (Eq. (6)) in the left panel and total energy conservation (Eq. (14)) in the right panel, both for Run F. The left panel depicts the time evolution of the total helicity $Q_5 + \frac{\alpha}{\pi \hbar c} \chi_m$

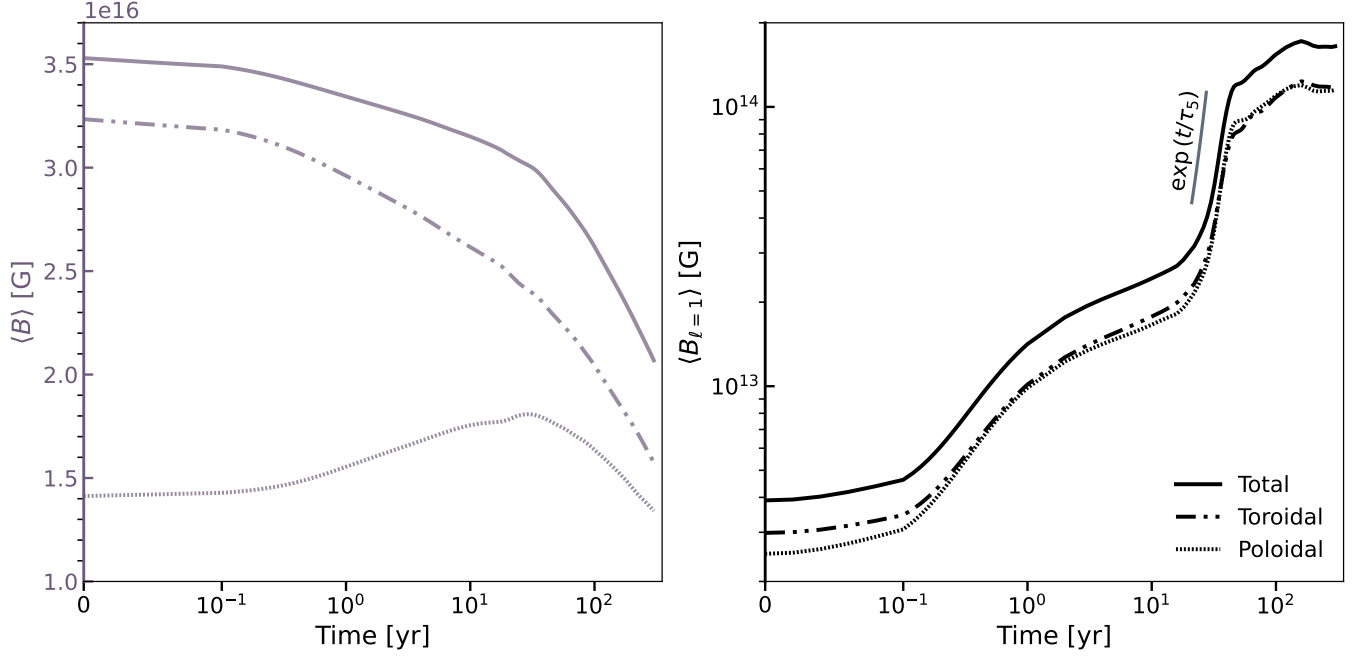


FIG. 4. Time evolution of the mean magnetic field (left panel) and the dipolar magnetic field (right panel) for Run F. Solid lines show the total field, dash-double-dotted lines the toroidal component, and dotted lines the poloidal component.

(dashed blue), the losses due to the spin-flip term at each time step $-\Gamma_5 \Delta t$ (dash-dotted orange), and the resulting axial charge Q_5 (dotted teal), which directly affects the magnetic field evolution. All quantities are dimensionless. The figure illustrates how the initial magnetic helicity generates a tiny (by 20 orders of magnitude) chiral asymmetry, Q_5 , which remains nearly constant over time due to spin-flip processes that counterbalance further growth. In the absence of spin-flip processes, Q_5 would grow until it is of the order of the magnetic helicity.

Moreover, the figure confirms that our simulations respect the generalized helicity conservation law (Eq. (6)): the change in total helicity is closely balanced by the spin-flip term, as predicted by theory. Minor discrepancies at early times (within the first few years) arise from numerical adjustments of the initial transient stage, and small surface helicity fluxes ($\propto \mathbf{E} \times \mathbf{A}$) caused by slight violations of the imposed boundary conditions. These surface contributions decay rapidly as the system self-adjusts over a few numerical iterations. Although reducing the timestep improves precision, it significantly increases computational cost. Nonetheless, helicity is conserved to a satisfactory degree for the purposes of this analysis.

To further ensure the physical robustness of our results and rule out numerical artifacts, the right panel of Figure 5 presents the total energy balance (Eq. (14)) for electromagnetic energy and the additional electron energy arising from chiral imbalance (see Equation (13)). The figure shows the time evolution of the key energy contributions: electromagnetic energy (E_{em}), Joule dissipation (Q_{tot}), Poynting flux (S_{tot}), and the total energy (black solid line), alongside the additional chiral terms, namely the chiral energy E_5 and the total spin-flip dissipation $\Gamma_{5\text{tot}}$, which are absent in standard Hall-MHD frameworks [25]. These chiral contributions are energetically subdominant. However, the primary chiral correction appears in the Joule dissipation term (Eq. (15)) via the $-k_5 \mathbf{B}$ modification to the electric field (Eq. (3)). This correction is crucial for accurate energy tracking and is dynamically nontrivial: in the absence of the Hall effect, it enhances dissipation when $k_5 \mathbf{B}$ is negative, suppresses it when positive, and can fully cancel magnetic dissipation when $\nabla \times \mathbf{B} \approx k_5 \mathbf{B}$. Overall, total energy is conserved within 5% throughout the simulation, with the magnetic energy gradually dissipating (mostly Ohmic dissipation), with the rest of the components being subdominant.

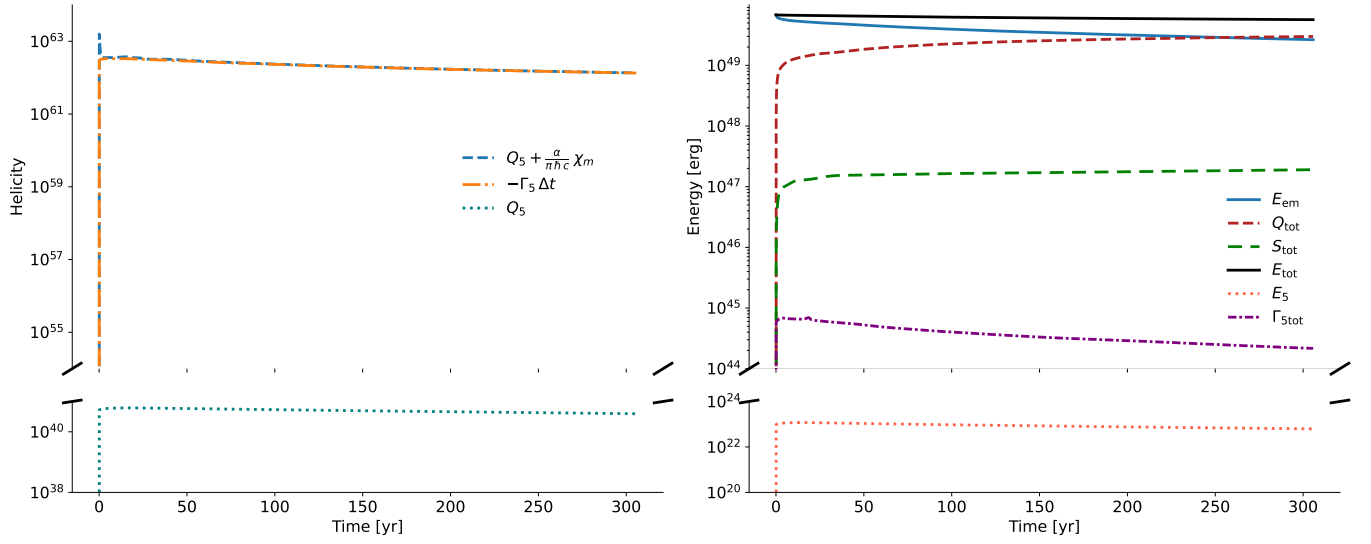


FIG. 5. Generalized helicity and energy conservation. Left panel (Eq. (6)): Time evolution of the total helicity $Q_5 + \frac{\alpha}{\pi \hbar c} \chi_m$ (dashed blue), the losses due to the spin-flip term at each time step $-\Gamma_5 \Delta t$ (dash-dotted orange), and the resulting axial charge Q_5 (dotted teal). All quantities are in non-dimensional form. Right panel (Eq. (14)): Time evolution of the electromagnetic energy E_{em} (solid blue), the Joule dissipation Q_{tot} (dashed red), the Poynting flux S_{tot} (dashed green), the chiral energy E_5 (dotted orange-red), the total flip term $\Gamma_{5\text{tot}}$ (dash-dotted purple), and the total energy (solid black).